

TITLE
AUTHORS
DATE

Abstract

This thesis studies the Wtb vertex structure, using data ATLAS data from top quark decays, derived from $t\bar{t}$ events. The events are reconstructed with missing transverse momentum, single lepton decay and at least four jets where two of those jets are tagged as b jets. The ATLAS Open Data, used in this thesis, was taken from pp collisions at a center-of-mass energy of 13 TeV, which corresponds to a integrated luminosity of 10 fb^{-1} . Angular asymmetries is used as the primary method for measuring the polarization of the W bosons, with a novel approach of fitting Delphes W polarization simulations to data taken from the ATLAS detector. The measured helicity fractions from Angular asymmetries are $F_0 = 0.634 \pm 0.016$, $F_L = 0.339 \pm 0.009$ and $F_R = 0.026 \pm 0.009$, with only statistical uncertainties considered, with angular asymmetries of $A_+ = 0.521 \pm 0.006$ and $A_- = -0.828 \pm 0.006$, deviating slightly from the Standard Model.

Contents

1	Introduction	4
2	Theory	5
2.1	Standard Model	5
2.1.1	Quantum Chromodynamics	6
2.1.2	Symmetries and Laws of Conservation	7
2.2	Momentum	8
2.2.1	Four-momentum	8
2.2.2	Transverse Momentum	9
2.3	Top Quarks	10
2.4	Coupling of W^+tb	11
3	Apparatus	13
3.1	LHC	13
3.2	ATLAS	14
3.2.1	The Inner Detector	14
3.2.2	Calorimeter	15
3.2.3	Muon Spectrometer	15
3.2.4	Data Collection	15
3.3	ROOT	16
3.4	Monte Carlo Simulation	16
4	Data Analysis	17
4.1	Angular Asymmetries	17
4.2	Template Method	17
4.3	Event Selection	18
4.3.1	B-tagging	18
4.4	Histograms from the ATLAS data	19
4.5	$\cos\theta^*$ reconstruction	21
4.6	Delphes data	21
4.7	Fitting to atlas data	23
5	Discussion	24
6	Conclusion	26

1 Introduction

The standard model (SM) of particle physics is very successful at describing the fundamental constituents of matter in our universe. Through experiments with particle accelerators, many of the theoretical details in the SM has been corroborated. To further test the theory larger accelerators are needed, which led to the construction of the large hadron collider (LHC), finished in 2008. Particles are collided together at high energy to probe the properties of the produced debris, hoping to discover new physics that deviates from the SM.

The top quark was discovered in 1995, by experiments done by CDF [2] and DØ [1]. It is the heaviest known fundamental particle, with a mass of $173.34 \pm 0.27 \pm 0.71 \text{ GeV}/c^2$, and its coupling strength to all the bosons are well predicted by the standard model. Because of its heavy mass and consequently short lifetime, it doesn't have enough time to bind with lighter quarks and form hadrons before it decays, which means that it effectively decays, to a good approximation, as a free quark. Measurements of the top quark's properties plays an important role in testing the Standard Model. Top quark production at LHC occurs via strong interactions, where they are produced in top, anti-top pairs. One test of the Standard Model, is the study of the Wtb vertex Lorentz structure and coupling, which is studied by looking at the decay products of top quarks. The top quarks decay, with almost 100% branching fraction, by weak interactions into W bosons and bottom quarks $t \rightarrow W + b$. The W bosons decay, into either a charged lepton and neutrino; $W \rightarrow l + \nu_l$, or into a quark, anti-quark pair: $W \rightarrow q' + \bar{q}$, as illustrated in the Feynman diagram Figure 1.

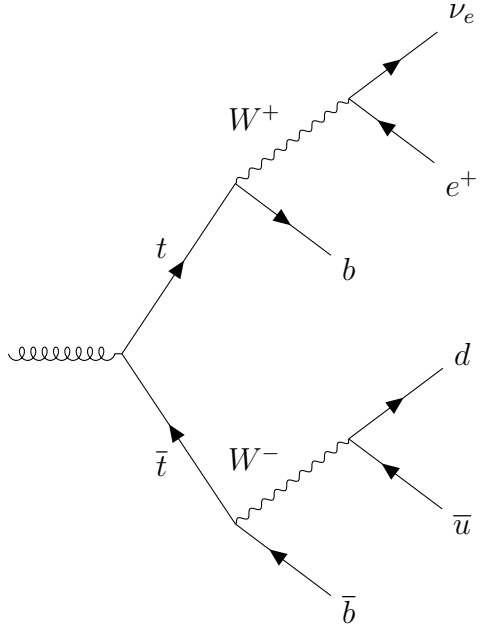


Figure 1: The Feynman diagram shows the chain of decay, that results in single leptonic decay, for pair $t\bar{t}$. The diagram illustrates the final product of the reaction; at least four jets and a lepton neutrino pair.

In this report, we are only looking at decays with a single lepton as decay product. The leptons we look at are either electrons or muons, and the collision will produce four jets, as evident from the diagram.

2 Theory

2.1 Standard Model

The Standard Model is a relativistic quantum field theory that describes three of the four fundamental forces, (the electromagnetic force, the strong force and the weak force), into a single theoretical framework. It contains all the known elementary particles, and how these particles interact with the different fields. The standard model manages to unify the electromagnetic (EM), and the weak force into different aspects of the same force called the electroweak force, while describing strong interactions through the framework of Quantum Chromodynamics.

The elementary particles can be split into two distinct categories, called

fermions and bosons. Fermions are defined by their spin, which is a half odd integer spin, but is exclusively 1/2 for all the elementary fermions of the Standard Model. They obey the pauli exclusion principle which means that two identical fermions can't occupy the same quantum state. The fermions are grouped into quarks and leptons, each with three generations or families based on their masses. All the fermions have an antiparticle associated with them, each with opposite charge, and apart from these antiparticle partners, there are a total of twelve known fermions, two leptons and two quarks in each family. The quarks that pair together in each generation are; the up and down quark, the charm and strange quark, and the top and bottom quark. The leptons, electron, muon and tau, each pair together with a neutrally charged neutrino.

In the SM, the fermions interact via gauge bosons, integer spin particles, which include the photon, gluon, W - and Z -boson, also called force carrier particles of the: electromagnetic force, the strong force and the weak force respectively. Quarks interact with the EM and the strong force, while leptons interact only with the electroweak force. Because neutrinos are neutrally charged, they will only interact via the weak force. Several unique features is found in weak interactions, such as parity violation (P), violation of charge conjugation (C), as well as a violation of the combined charge conjugation and parity symmetry (CP). Weak interactions do obey the combination of charge conjugation, parity, and time reversal symmetry.

2.1.1 Quantum Chromodynamics

Quantum chromodynamics (QCD), is the theory of the strong interaction, which binds the quarks together. In the year 1964, physicist Murray Gell-Mann and his PhD student George Zweig, proposed that baryons and mesons could be explained by the existence of smaller triplet particles[14]. Since the Pauli exclusion principle forbids any fermions from inhabiting the same state, leading to the development of the concept of color in 1973[13] by physicists Harald Fritzsh, Heinrich Leutwyler and Murray Gell-mann, suggesting that these quarks had additional conserved quantum numbers, later named color charge.

In QCD, each quark is associated with a color charge that confines the quark via the strong interaction to other quarks to make up a total color charge that is neutral. While the color charge isn't physically related to actual colors, the way they mix together, is analogous to the way we mix the colors green, red and blue, as well as their anti colors, magenta, yellow and

cyan. Because of these properties, quarks can bind together in groups with odd number of quarks with at least three to form baryons, or an even number of at least two to form mesons.

If enough energy is added to stretch one of the quarks away from the rest, the gluon field breaks, and a new quark and anti quark pair is created. This process of creating new quark, anti quark pairs, by stretching the gluon field between them is the result of violent inelastic collisions, which creates these jets of quarks, anti quarks.

2.1.2 Symmetries and Laws of Conservation

In the year 1971, Emmy Noether showed that any conservation law is associated with a continuous symmetry of the Lagrangian[17]. The conservation laws of classical physics are the result of them being invariant with respect to their canonically conjugate quantities. The conservation of energy, linear momentum and angular momentum, stems from their invariance in time, space and angles respectively. This implies that the laws of physics are independent of the time, the location and the orientation in space.

Another symmetry, that is very important for quantum mechanics, is the reflection symmetry, called parity. A wave function can have positive or negative parity depending on whether or not it changes sign under parity transformation. For the laws which are invariant under reflection in space, the parity quantum number P is conserved, while in relativistic quantum mechanics, we need to ascribe an intrinsic parity to particles and antiparticles.

Group theory gives the tools to study these symmetries more elegantly, and has become particularly useful to describe symmetries of quantum mechanics, where degenerate eigenstates furnishes irreducible representations of a group. In studying these groups, we can discover other conserved quantities in the interactions of the EM, the weak or the strong force.

The unitary group $U(1)$, leads to conservation of charge in EM and strong interactions, as well as the conservation of lepton number, as far as we know in all interactions. Certain particles behave practically identically with respect to the strong or the weak interactions, these properties are studied through irreducible representations of the group $SU(3)$, and are characterized by strong and weak isospin, which are also conserved.

The Dirac equation extends the Schrödinger wave equations, to include the effects of special relativity. The solution to this equation shows that for relativistic particles, where $\beta = v/c \rightarrow 1$, the projection of a particle's spin onto the direction of their momentum is conserved. This conserved quantity is called helicity[21, p. 63] and is defined as

$$h = \frac{\mathbf{s} \cdot \mathbf{p}}{|\mathbf{s}| \cdot |\mathbf{p}|}, \quad (2.1)$$

where \mathbf{s} is the spin, and \mathbf{p} is the momentum of the particle. For spin 1 particles, the Gauge bosons, the particle can take on three distinct helicity values, $h = -1$, $h = 0$ and $h = 1$, which corresponds to left-handed, longitudinal and right-handed respectively.

Chirality is a fundamental property of a particle determined by representation theory. In the relativistic limit the distinction between helicity and chirality disappears, as the mass term mc^2 becomes negligible compared to the total energy. The weak force will only interact with left-chiral particles and right-chiral antiparticles. The operator of an interaction that describes the exchange of a boson, can have both vector V and axial vector A nature. If it has both a vector and an axial part, as in the case of weak interactions, parity is violated, while maximum parity violation occurs when both the contributions becomes equal magnitude.

After the discovery of parity violation and charge conjugation, by physicist C.S Wu[25], it was believed by physicists that CP-symmetry, the combination of charge conjugation symmetry and parity, was a true symmetry of the Standard model, until that too was violated in weak decay of neutral kaons, forcing physicists to reformulate the electroweak interaction in the Standard Model. The Cabibbo-Kobayashi-Maskawa (CKM) matrix explains how the flavour eigenstates of the quarks are related to the mass eigenstates, and is a 3×3 unitary matrix, with four independent parameters: three real angles and an imaginary phase[21, p. 153]. The imaginary phase gives rise to CP violation, but the matrix preserves CPT symmetry.

2.2 Momentum

2.2.1 Four-momentum

The data collected in LHC collisions, allows us to reconstruct the 4-vector of momentum for the involved particles. This 4-vector is a four component tensor, made up of an ordinary 3-vector for relativistic momentum \mathbf{p} , and the

relativistic energy term, E^2/c^2 , as its first component. Working in natural units, where we set $c = 1$, our 4-vector will be given as

$$p = \begin{pmatrix} E^2 \\ \mathbf{p} \end{pmatrix}. \quad (2.2)$$

The dot product of two 4-vectors is given by $p \cdot p' = EE' - \mathbf{p} \cdot \mathbf{p}'$, where $\mathbf{p} \cdot \mathbf{p}'$ is the ordinary dot product of two 3-vector momentum. From special relativity, we know that $E^2 - |\mathbf{p}|^2 = m^2$, so from the dot product, we get that $p^2 = m^2$. Other vector operations on a 4-vector is similar to those same vector operations on a 3-vector. The quantity

$$s = (p + p')^2 = (E + E')^2 - (\mathbf{p} + \mathbf{p}')^2 \quad (2.3)$$

is conserved, and is the center-of-mass energy squared of the system. It is the energy available to create new particles, or probing the properties of particles.

2.2.2 Transverse Momentum

In LHC experiments, the protons gets smashed together in head-on collisions at nearly the speed of light. Since the protons momenta are parallel to the beam axis, conventionally defined as the z -axis their total momentum in the xy -plane, the transverse momentum p_T , is zero. The jets scatter off in new directions, at angles given by the polar angle θ , and the azimuthal angle φ . The polar angle is defined as the angle of the jet, with respect to the z -axis, in the xz -plane, while the azimuthal angle is defined as the angle of the jet, with respect to the x -axis in the xy -plane, as seen in Fig. 2.

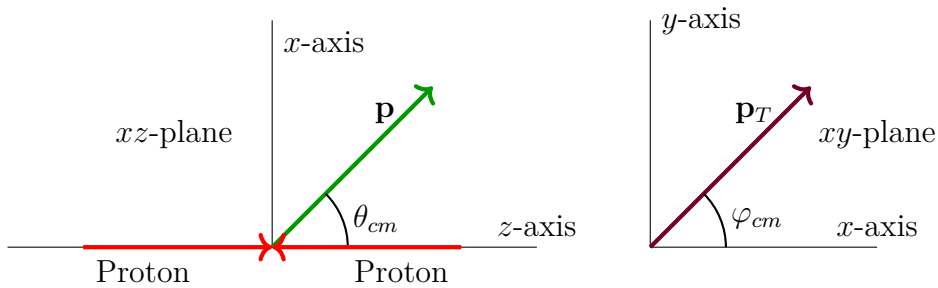


Figure 2: The figure shows the momentum traveling parallel to the beam axis, and the transverse momentum, each with their respective angles.

In cylindrical detectors, it is useful to use another magnitude called pseudorapidity, which ranges from values between $(-\infty, \infty)$. Pseudorapidity is related to the polar angle, and is defined as:

$$\eta = -\ln \left(\tan \left(\frac{\theta}{2} \right) \right). \quad (2.4)$$

Not all particles are, or can be detected by the detectors, but their existence is still well understood through the conservation of momentum. At $v \rightarrow c$, the momentum $|\mathbf{p}| \approx E$, and the missing transverse momentum E_T^{miss} is defined as the transverse momentum that is not detected by the detector, but calculated as the momentum for which the total momentum will become zero [24].

2.3 Top Quarks

The top quark is the third generation up-type quark in the SM, with a charge of $+2/3e$, and the greatest mass of all the known elementary particles. Top quark has a weak two-body decay and its decay can be analysed from the Cabibbo-Kaboyashi-Maskawa matrix (CKM). The diagonal part of the CKM matrix, shows quarks transition predominantly within their own family, with very little deviation from unity. This is especially true for the top quark, where top quarks decays into bottom quarks and W bosons 99.8% of the time. Because the top quark decays as a free quark, we can use the polarization as an observable, because its spin will be preserved in the decay product.

There are two primary mechanisms for the production of top quarks at the LHC, a single top via weak interactions, or the pair production via the strong force. The pair production of top quark is a QCD effect, which takes place by gluon fusion $gg \rightarrow t\bar{t}$ and quark-antiquark annihilation $q\bar{q} \rightarrow t\bar{t}$. The branching fraction of each of the pair production processes, is related to the center-of-mass energy, for which gluon fusion dominates at the LHC at about 86% of the production[23].

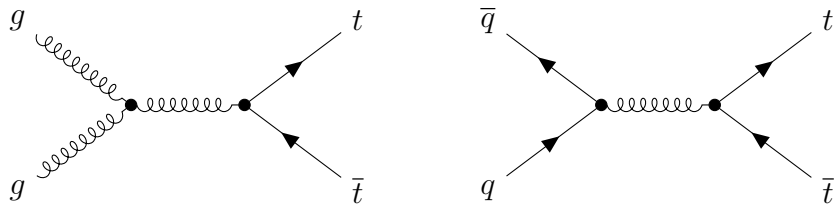


Figure 3: A Feynman diagram of the two main production processes $gg \rightarrow t\bar{t}$ on the left, and $q\bar{q} \rightarrow t\bar{t}$ on the right. Both production mechanisms are results of strong interactions.

2.4 Coupling of W^+tb

The leptonic decay of the W -boson, can decay into either of the three leptonic families, with nearly equal branching ratios. The τ lepton is also very unstable and has too short a lifetime, so it does not get tagged in this thesis. τ -particles that decay by weak interaction into electrons, $\tau^+ \rightarrow e^+ \nu_e$, or muons, $\tau^+ \rightarrow \mu^+ \nu_\mu$, are tagged as part of the single lepton channel.

The W -boson couples only to left-handed fermions, or right-handed anti-fermions, giving Wtb vertex a (V-A) structure. In the Standard Model we expect that the W -boson and b -quark from top decay, arrange such that chiral structure of the couple vertex is fulfilled. Because of parity violation, the events with positive helicity (right polarized) gets suppressed, while events with negative (left polarized) and longitudinal helicity dominates.

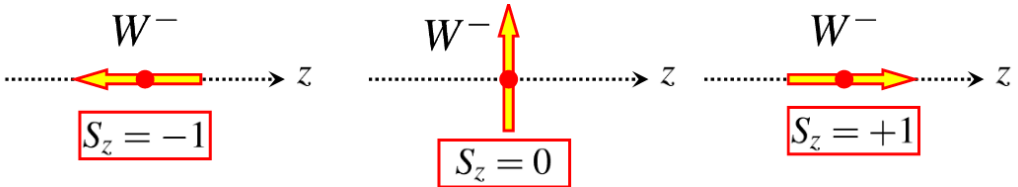


Figure 4: The figure illustrates W -boson with negative, zero and positive helicity, corresponding to a left, longitudinal and right handed polarization. The right handed polarization will be heavily suppressed because of the (V-A) structure of the Wtb vertex.

The fraction of; longitudinally F_0 , left F_L or right F_R polarized W -bosons which are produced from top quark decay, we refer to as helicity fractions. In the Standard Model we can determine these fractions with quantum chromodynamics, in next to next to leading order (NNLO) calculations to be $F_0 = 0.687 \pm 0.005$, $F_L = 0.311 \pm 0.005$ and $F_R = 0.0017 \pm 0.0001$ [10]. The experimental method to extract these fractions is by studying the angular decay distribution of the leptonic decay products of the top quark. The angular distribution is given by:

$$\frac{1}{\Gamma} \frac{d\Gamma}{d \cos \theta^*} = \frac{3}{8} (1 - \cos \theta^*)^2 F_L + \frac{3}{4} \sin^2 \theta^* F_0 + \frac{3}{8} (1 + \cos \theta^*)^2 F_R. \quad (2.5)$$

Where θ^* is the helicity angle, which is defined as the angle between the decayed lepton momentum direction, and the reversible momentum direction of the b -quark decay from the same top quark, viewed from a reference frame

with W at rest[16]. From the 4-vectors of the lepton and b -jet, we can find the $\cos \theta^*$ from the following expression:

$$\cos \theta^* = \frac{p_l \cdot p_b - E_l E_b}{|\mathbf{p}_l| |\mathbf{p}_b|} \simeq \frac{2M_{lb}^2}{m_t^2 - M_W^2} - 1. \quad (2.6)$$

Here p_l and p_b are the four momentum vectors of the lepton and the bottom quark respectively. M_{lb} is the invariant mass of the lepton and bottom quark system. The dependence is shown in Fig. 5 for the three distribution separately, and for the SM, with the above-mentioned NNLO helicity fractions.

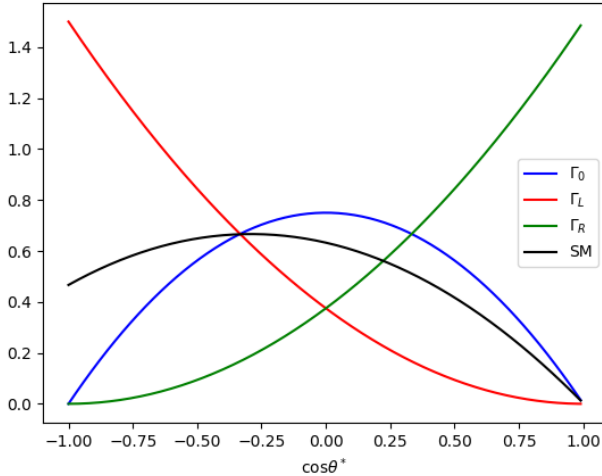


Figure 5: The predicted $\cos \theta^*$ angular distribution for helicity fractions. The distributions for F_0 , F_L and F_R are normalized, and are given by the blue, red and green line respectively. The black line is the sum of the three contributions, but with helicity fractions given according to SM predictions.

Another approach to obtaining the polarization states the W -bosons, is done by counting the number of events with a specific $\cos \theta^*$, then use angular asymmetries, A_- , and A_+ , defined as

$$A_{\pm} = \frac{N(\cos \theta^* > z) - N(\cos \theta^* < z)}{N(\cos \theta^* > z) + N(\cos \theta^* < z)}, \quad (2.7)$$

with $z = \pm(1 - 2^{2/3})$, to choose asymmetries involving only dependence on F_0 and F_L for A_+ , or F_0 and F_R for A_- . The helicity fractions for the W

boson, can then be obtained by,

$$F_R = \frac{1}{1-\beta} + \frac{A_- - \beta A_+}{3\beta(1-\beta^2)}, \quad (2.8)$$

$$F_L = \frac{1}{1-\beta} - \frac{A_+ - \beta A_-}{3\beta(1-\beta^2)}, \quad (2.9)$$

$$F_0 = -\frac{1+\beta}{1-\beta} + \frac{A_+ - A_-}{3\beta(1-\beta)}, \quad (2.10)$$

where $\beta = 2^{1/3} - 1$. The values for angular asymmetries is calculated in SM NNLO as $A_+ = 0.537 \pm 0.004$ and $A_- = -0.841 \pm 0.006$ [5, p. 24].

3 Apparatus

3.1 LHC

In the Large Hadron Collider, top quarks are mainly produced through violent collisions of protons, causing gluon-gluon fusion, which produces top, anti-top pairs $gg \rightarrow t\bar{t}$. The data used in this thesis, is from the 2016 run at LHC, with a centre-of-mass energy of $\sqrt{s} = 13\text{TeV}$, which corresponds to an integrated luminosity of 10 fb^{-1} [22]. At these energies, the protons are accelerated close to the speed of light before their collisions in the ATLAS detector.

This process starts, when protons are generated from an ion source in the linear accelerator, LINAC2, then gets injected into the LHC, through a series of smaller synchrotron accelerators, as Fig. 6 illustrates; Proton Synchrotron Booster (PSB), Proton Synchrotron (PS) and Super Proton Synchrotron (SPS) [11, p. 135]. The LHC receives bunches from SPS, containing many protons in each bunch, effectively increasing the cross-sectional area for collisions to occur. In order to prevent energy loss due to synchrotron radiation, the LHC was built to be the largest particle accelerator in the world, which has allowed it to reach higher energies than other accelerators. At these energies, more events happen inside the detector, described by the following equation:

$$N = \sigma \int L dt, \quad (3.1)$$

where N is the number of expected events, σ is the cross-sectional area of the events, and $\int L dt$ is the integrated luminosity.

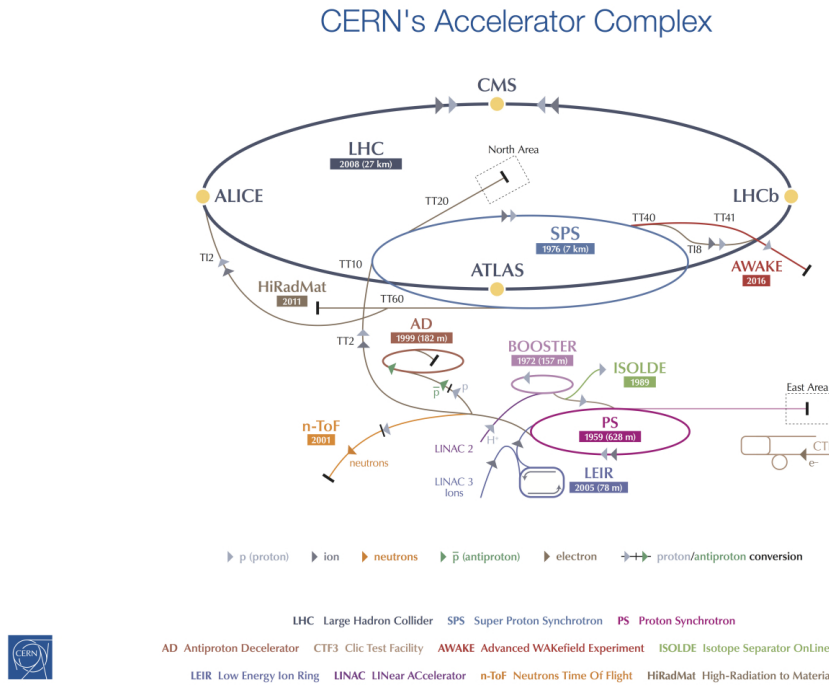


Figure 6: The scheme shows the accelerator and detector layout at CERN [15].

3.2 ATLAS

The ATLAS detector consists of multiple primary components, each with their own subcomponents or subsections.

3.2.1 The Inner Detector

The purpose of this component is to measure charge and momentum, including its direction, of the detected particle. It consists of three subcomponents.

Pixel Detector The pixel detector consists of approximately 92 million electronic channels. It's used for identification and reconstruction of secondary vertices from decay of particles containing a b-quark or for b-tagging jets. The pixel detector covers pseudorapidity range $|\eta| < 2.5$

Semiconductor Tracker The Semiconductor tracker is a silicon microstrip tracker consisting of 4088 two-sided modules and over 6 million readout

strips. These readout strips are distributed every $80\mu\text{m}$ which allows recording of the position of charged particles to an accuracy of $17\mu\text{m}$

Transition Radiation Tracker. The transition radiation tracker is a drift tube tracker which consists of a straw with 4mm diameter and 0.03mm diameter tungsten wire, coated with 0.5–0.7mm gold. The tube is filled with a mixture of Xe, CO₂ and O₂ gasses. When charged particles travel through the tube the gas gets ionized, which frees electrons from the gas that move to the gold wire. The negative charge measured on the wire can be used to distinguish which charged particle ionized the gas. [9]

3.2.2 Calorimeter

Calorimeters measure the energy of particles by absorbing them. There are two types of calorimeters used in the ATLAS detector; the Electromagnetic Calorimeter (ECal) and Hadronic Calorimeter (HCal). ECal measures charged particles and photons.

The HCal consist of scintillator plates that radiates light when exposed to a charged particle. When a hadron passes through a scintillator plate it produces a shower of particles which then makes the scintillator radiate light. The intensity of the radiated light can then be analysed to measure the energy of the hadron. [3]

3.2.3 Muon Spectrometer

The muon spectrometer is on the outer part of the ATLAS detector it operates in the pseudorapidity range $|\eta| < 2.7$. Muons usually pass through the inner detector and the calorimeters undetected, which is why the muon spectrometer is located on the outside as other particles will have been stopped earlier in the detector. The muon spectrometer consists of tubes, much like the transition radiation tracker, that contains a gold wire which is surrounded by a gas. When muons go through these tubes they interact with the gas and leave behind a trail of ions and electrons which drift towards the gold wire in the centre. By detecting the starting point of these trails, and measuring the time it takes to reach the gold wire, it is possible to determine the position of the muon. The Muon Spectrometer can be seen in Figure 7 [7]

3.2.4 Data Collection

The detector generates 60 terabytes of data per second from the 1.7 billion collisions taking place in the detector in that time frame. However, only a

small sample of the raw data is necessary to reconstruct the collisions. To make the data more manageable ATLAS uses a two-level trigger system to only save the most important data. The first part of the trigger system is hardware based, and can at most save 100 000 events per second, which then gets passed on to the software based High-Level Trigger. After passing through both triggers, only approximately 1000 events out of the initial 1.7 billion are saved for later analysis.[8]

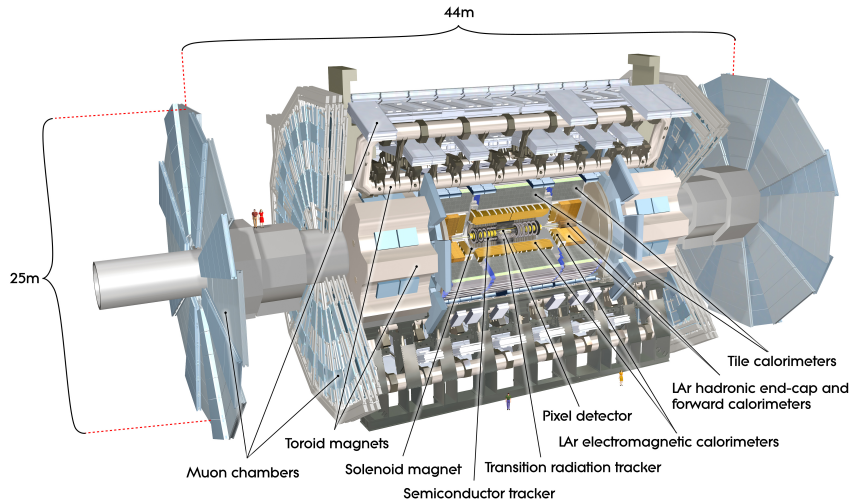


Figure 7: A computer generated image of the ATLAS detector [20]

3.3 ROOT

ROOT is a framework used for storing and processing data in high energy physics. ROOT is primarily written in the programming language c++. Data in ROOT files are stored in a tree format, the file itself is a compressed binary file. [6]

3.4 Monte Carlo Simulation

Monte Carlo (MC) simulation is used in modelling the signal and background processes expected at the LHC. For the 13 TeV Atlas Open Data used in this thesis, this process follows four steps; starting with an event generation which uses an MC generator to mimic the initial pp collision. In the second step, detector simulation, the geometry of the ATLAS detector and its material properties gets simulated. The digitization step, follows the previous step by simulating the responding signals in read-out data, written in a format

compatible with real output of the detector. Finally, these data can be used to reconstruct the collisions, particle trajectories and subsequent products.

In The 13 TeV ATLAS Open Data set, there are several SM processes which are modelled using MC simulations. For the purpose of this report, the MC simulations on top-quark-pair production was used alongside real data taken from the detector, to compare theory with real data [19].

4 Data Analysis

4.1 Angular Asymmetries

For measurements of angular asymmetries A_{\pm} from equation (2.7), the $\cos \theta^*$ distribution was split into three non-uniform bins with events above and below $z_{\pm} = \pm(1 - 2^{\frac{2}{3}})$ given by; $N_1 = N(\cos \theta^* < z_-)$, $N_3 = N(\cos \theta^* > z_+)$ and N_2 being the remaining events. Applying these parameters to the simulated data, correction factors e_1 and e_3 were obtained by comparing the simulated data to the Standard Model expectation, then solving the system of equations obtained from (2.7).

$$A_+^{SM} = \frac{(e_3 N_3 + N_2) - e_1 N_1}{e_1 N_1 + e_2 N_2 + e_3 N_3} \quad (4.1)$$

$$A_-^{SM} = \frac{e_3 N_3 - (e_1 N_1 + N_2)}{e_1 N_1 + e_2 N_2 + e_3 N_3} \quad (4.2)$$

Solving for the correction factors the following values are obtained.

$$e_1 = (1.515 \pm 0.065) \times 10^{-2} \quad (4.3)$$

$$e_3 = (5.390 \pm 0.081) \times 10^{-2} \quad (4.4)$$

These correction factors obtained from simulation is then applied to the $\cos \theta^*$ distribution from the ATLAS data.

Leading to the angular asymmetries $A_- = -0.828 \pm 0.006$ and $A_+ = 0.521 \pm 0.006$, resulting in the helicity fractions $F_0 = 0.634 \pm 0.016$, $F_L = 0.339 \pm 0.009$ and $F_R = 0.026 \pm 0.009$.

4.2 Template Method

Pythia was used to generate three files containing left, longitudinal and right-handed polarizations of the W-boson separately. These files were then run

through Delphes, which simulates the ATLAS detector response and uses that to reconstruct the particles. Cuts were applied in ROOT matching the event selection criteria defined in section 4.3 to filter out background data. The templates were then combined and fitted to the real $\cos \theta^*$ distribution from the ATLAS detector, giving us the three helicity fractions F_L , F_R and F_0 .

4.3 Event Selection

In order to identify the top-quark-pair production, as seen in figure 1, several cuts in the data were implemented. The criteria are as follows [22].

- Only one electron or muon in the final state with $p_T > 30\text{GeV}$
- Missing transverse momentum $E_T^{miss} > 30\text{GeV}$
- Transverse mass of the W-boson $M_T^W > 30\text{GeV}$
- At least four jets with $p_T > 30\text{GeV}$ and $|\eta| < 2.5$, with exactly two of these being b-tagged
- Electrons are required to have $|\eta| < 2.47$ aside from $1.37 < |\eta| < 1.52$
- Muons are limited by $|\eta| < 2.50$

4.3.1 B-tagging

To study the Wtb structure, a mechanism to identify the b -jets from the other detected jets is required. First the jets are detected, b -hadrons, c -hadrons or light-flavour jets, then their trajectories (tracks) are reconstructed in the inner detector. Once a jet has been found, the jets containing b -hadrons are then identified by a combination of three distinct algorithms. Hadrons containing b -quarks have a long enough lifetime to fly a measurable distance before it decays, and can be exploited to built lifetime-based tagging algorithms. The impact parameter based algorithm, IP3D, uses transverse and longitudinal impact parameter significances of each track within a jet, the SV reconstructs the secondary vertex within the jet and decay chain multi-vertex algorithm (JetFitter) reconstructs the full b -hadron decay chain.

To better discriminate between jets, a Boosted Decision Tree (BDT) algorithm called MV2c10, which uses the Root Toolkit for Multivariate Data Analysis (TMVA), is used to make cuts that discards most of the background components, the c - and light-flavoured jets. For this report, a b -jet efficiency

rate of 70% is used, which corresponds to a BDT cut value of 0.8244. This efficiency rate originates from samples of simulated $t\bar{t}$ events with a c - and light-jet rejection factor of nearly 400[18]. At these cuts, most of the c -jets and light-flavoured jets gets rejected, while still maintaining most of the b -jet data.

4.4 Histograms from the ATLAS data

ROOT defines the function `SetPtEtaPhiE`, which is used in accordance to section 2.2 as seen in equation (4.5).

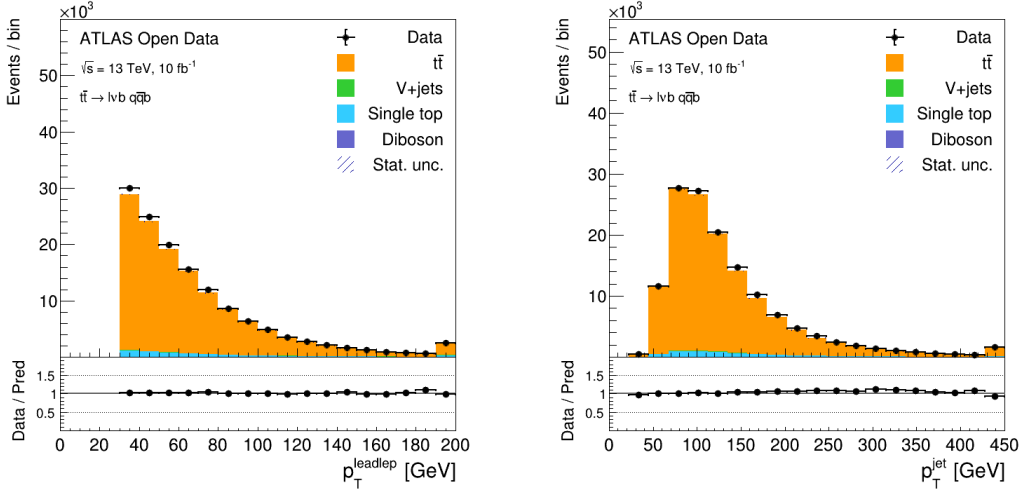
$$p(\mathbf{p}_t, \eta, \phi, E) = \begin{pmatrix} |\mathbf{p}_t| \cos(\phi) \\ |\mathbf{p}_t| \sin(\phi) \\ |\mathbf{p}_t| \sinh(\eta) \\ E \end{pmatrix} \quad (4.5)$$

Only a single lepton should be present in the events, after the identification of top-quark pair production. This allows the first lepton in the event to be used as the leading lepton. Due to the nature of the decay, described in Section 2.4, the tagged lepton can be either an electron or a muon. This information is used in the construction of the Lorentz vector for the lepton, from which the transverse momentum is plotted in Fig. 8a.

In the ATLAS Open Data, the reconstruction of the tracks, and calculation of the transverse momentum of jets, is already given. The jets in the event are ordered, which provides information about the leading jet simply by accessing the first one. Good jets are decided on the requirements given in Section 4.3, and the momentum plotted in Fig. 8b.

The missing transverse energy, E_T^{miss} , is also given, calculated by consideration of momentum conservation, in accordance with what is described in Section 2.2.2. The missing transverse energy is then plotted if the given event satisfies all the criteria given in Section 4.3. The energy was plotted in the appropriate units in Figure 9a.

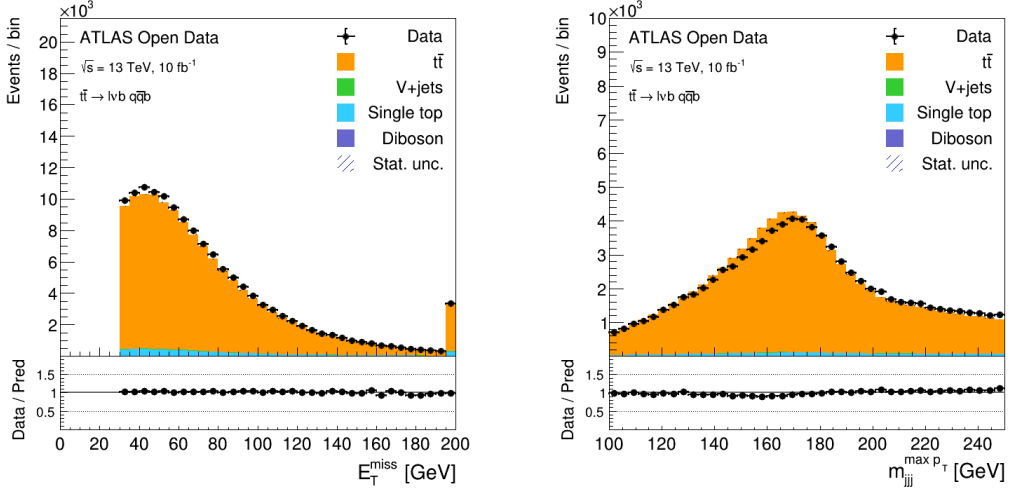
The top quark mass can be calculated by finding the combination of three jets, of which one is a b -jet, with the highest transverse momentum, and taking the mass of the whole three jet system. These three jets are the ones produced by the \bar{t} -quark in the lower part of the Feynman diagram seen in Figure 1. Once the top quark mass is found it can be plotted, as seen in Figure 9b. The peak of this histogram should then be compared to the value from the standard model, which is 172.76 ± 0.30 GeV[27].



(a) Lead lepton transverse momentum for both single-electron and single-muon channel.

(b) Lead jet transverse momentum for both single-electron and single-muon channel.

Figure 8



(a) Missing transverse energy for both single-electron and single-muon channel.

(b) Top quark mass from the ATLAS data.

Figure 9

4.5 $\cos \theta^*$ reconstruction

Reconstruction of $\cos \theta^*$ from the data given in the Lorentz 4 vectors, was accomplished by equation (2.6). Since only two b -jets is tagged, the b -jet associated with the leptonic decay was decided by the method of exclusion, once the b -jet associated with the other jets was identified. The reconstructed $\cos \theta^*$ is plotted in Figure 10 below.

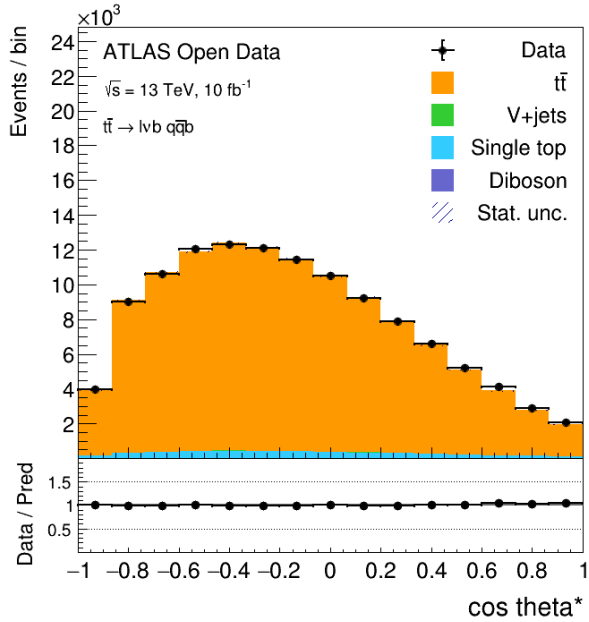


Figure 10: Reconstructed $\cos \theta^*$ from ATLAS data.

4.6 Delphes data

Before the criteria from Section 4.3 were applied to the Delphes data, a sanity check was performed on the generated truth data, to assess whether it matches with the theoretical analytical function plotted in Figure 5. The three plots are displayed below for each of the three polarizations in Figures 11.

To reconstruct the helicity distributions which would be found from measurements, the criteria performed on the ATLAS data, from Section 4.3, were matched on the Delphes data, to isolate the equivalent usable data, gotten from the ATLAS detector. The Figures 12 shows the three helicity distributions after the cuts.

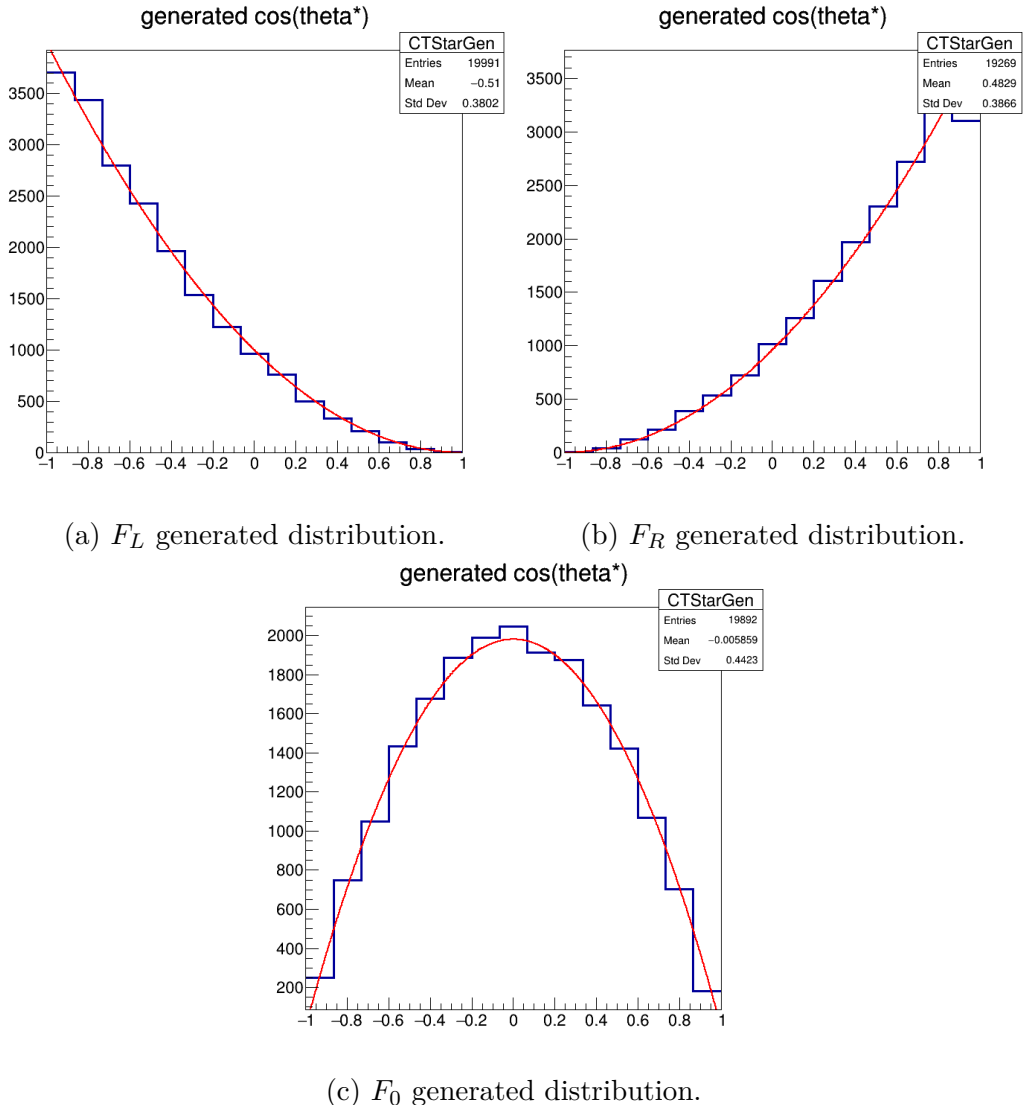


Figure 11: The figures shows the truth data of the generated F_L , F_R and F_0 distributions, with a sample of 20000 events, using Delphes fast simulations to generate.

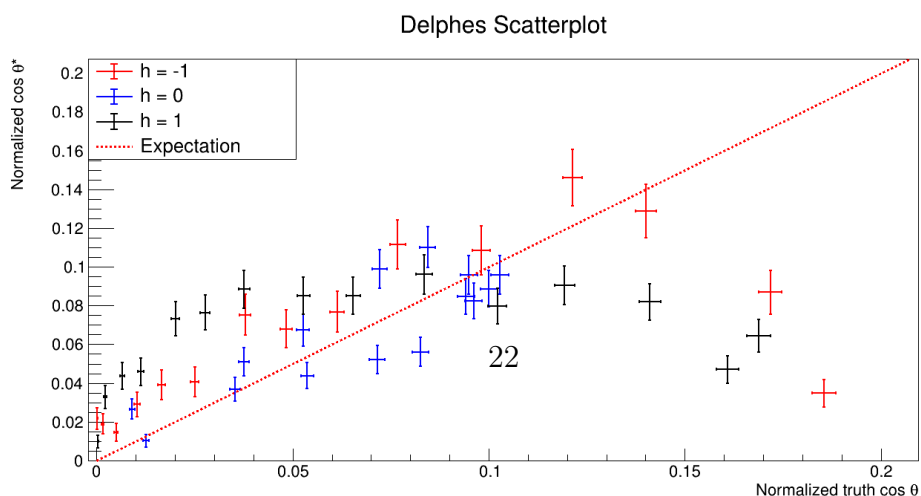


Figure 14: Every point represents a bin. The x -value is the normalized truth value, and the y -value is the normalized value after the cuts in the data have

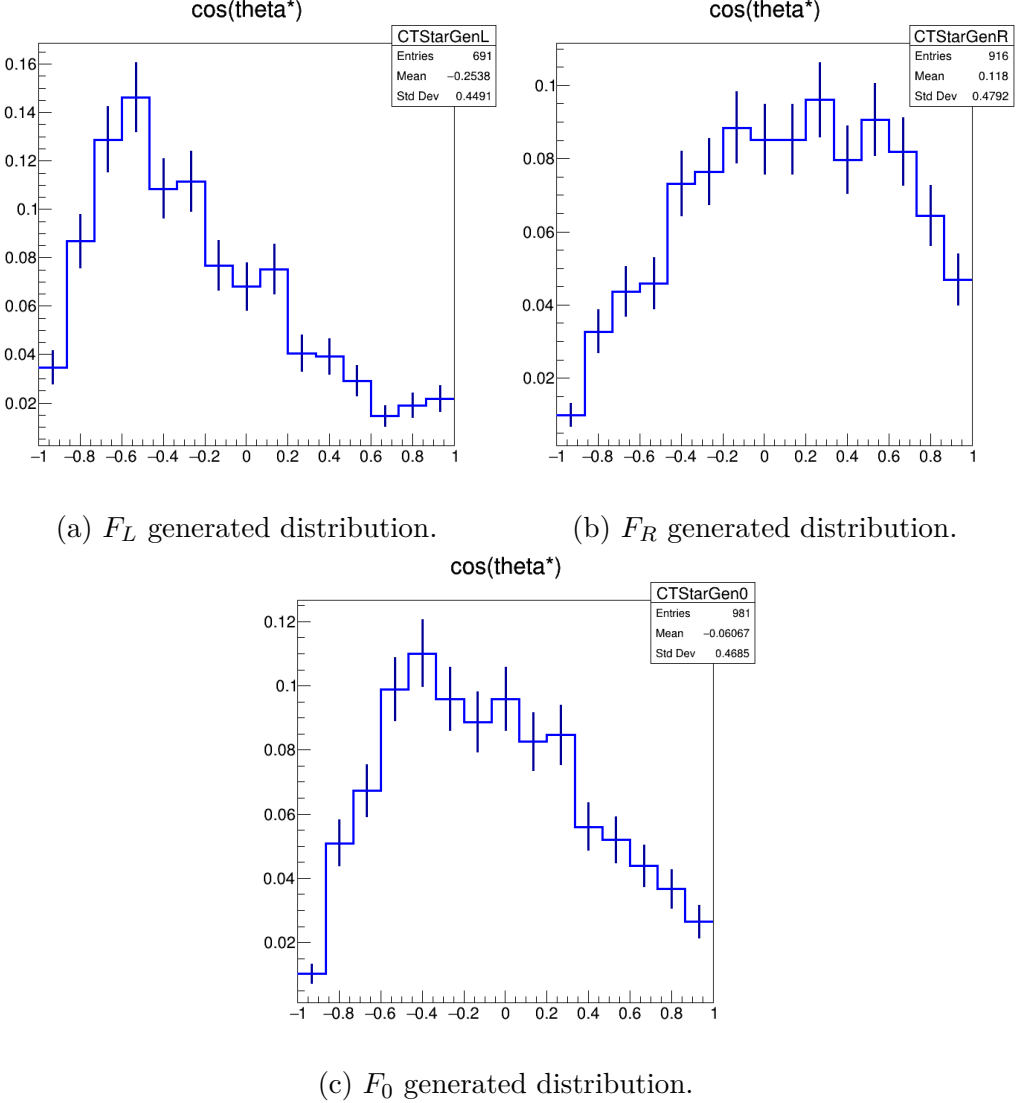


Figure 12: The figures shows the reconstructed Delphes $\cos \theta^*$ of the generated F_L , F_R and F_0 distributions, with a sample of 20000 events, using Delphes fast simulations to generate, and similar cuts to the ones made on the Open ATLAS data.

4.7 Fitting to atlas data

The histograms shown in Fig. 12, is fitted by a linear combination of parameters, to the histogram containing the ATLAS data. Figure 15 displays the fitted data, and below is listed the obtained parameters, corresponding to the helicity fractions, alongside the error associated with the iterative approach

$h = -1$	$h = 0$	$h = +1$	Sum
3.457%	4.932%	4.754%	4.375%

Figure 13: Efficiency table calculated by dividing the histogram entry count by its corresponding truth value histogram entry count.

to the fit.

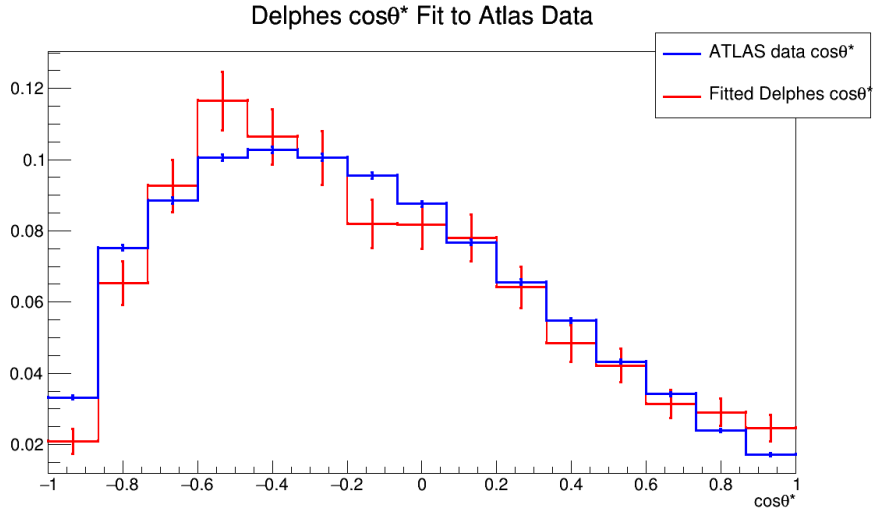


Figure 15: Reconstructed Delphes $\cos \theta^*$ fitted to the $\cos \theta^*$ from ATLAS data.

```

FCN=1963.72 FROM MIGRAD   STATUS=CONVERGED   61 CALLS      62 TOTAL
                           EDM=2.23898e-18   STRATEGY= 1      ERROR MATRIX ACCURATE
PARAMETER    VALUE        ERROR        STEP SIZE     1st DERIVATIVE
F_0          5.11016e-01  1.71117e-02  6.08806e-05  -5.60212e-07
F_L          4.41250e-01  9.31108e-03  6.00363e-05  -6.62772e-07
F_R          3.13704e-02  9.18531e-03  5.33415e-05  -3.72978e-07
CHI2 : 1963.72

```

5 Discussion

Due to the limitations of the released 13 TeV Open Datasets, it was not possible to analyse the helicity fractions' angular distributions through the ATLAS data, which lead to the utilization of Delphes. The deviation between the predicted SM values for the helicity fraction, and the value obtained through the fitting, is possibly the result of systematic errors when attempting to fit

Delphes simulated spin orientation, to the data obtained from the LHC Open ATLAS run in 2016. Since Delphes runs a fast-simulation, it is not designed to be used in parallel with data taken from advanced detector studies. This analysis consequently serves as a test for this novel approach of combining Delphes simulations with data taken from ATLAS detector. While similar cuts were attempted to be implemented on the Delphes' truth-information, due to the absence of the b-tagging MV2c10 algorithm in Delphes, cuts were made using 80–85% efficiency instead [4].

However, perhaps the greatest source of errors is a consequence of statistical errors, due to the small event samples surviving the cut on the given Delphes data, an efficiency of less than 1/20. Figure 14 illustrates the effect of the cuts on the truth data, where the normalized data of Fig. 11, is plotted out of one axis, and the data from Fig. 12 is plotted out of the other. The values for the reconstructed left and right-handed distributions diverge from the truth values, at values with higher density of events, corresponding to the corners of the truth distribution. As a result of time constraints, and the large storage space required to simulate a sufficient number of Delphes events, information about the W polarization was instead obtained by the method of angular asymmetries, described in Section 2.4.

For measurements of angular asymmetries, the error was found, using first order error propagation on equation (2.7). The statistical error of this approach, was significantly smaller, due to the fact that the data was taken exclusively from the Open ATLAS Data, which had a much larger data sample than the Delphes simulations.

The reconstructed $\cos \theta^*$, from the ATLAS data, used in both methods, had significant entries in overflow. The theoretical $\cos \theta^*$ was compared to the approximation, but no significant differences appeared between the two, refuting the possibility that overflow stemmed from the approximation. This overflow was ignored in the fitting process, as only data remaining within the physically possible range from -1 to 1, was considered in the analysis. The Delphes data for the helicity distributions, had substantially less overflow, than data from Open ATLAS, which also motivated the decision to only fit within the parameter -1 to 1.

6 Conclusion

A measurement of the polarization of W bosons, from top quark pair events decay to single lepton channels, was presented using data collected from Open ATLAS pp collision at $\sqrt{s} = 13\text{TeV}$, corresponding to an integrated luminosity of 10 fb^{-1} . The helicity fractions obtained from angular asymmetries are $F_0 = 0.634 \pm 0.016$, $F_L = 0.339 \pm 0.009$ and $F_R = 0.026 \pm 0.009$. Due to the limitations of the Open Atlas Data [22], only statistical uncertainties were considered, leaving the possibility of larger systematic uncertainties. The measured helicity fractions deviated slightly from the SM expectation values, but this could be the result of lack in systematic uncertainties, or discarding the overflow.

References

- [1] S. Abachi et al. “Observation of the Top Quark”. In: *Physical Review Letters* 74.14 (Apr. 1995), pp. 2632–2637. ISSN: 1079-7114. DOI: 10.1103/physrevlett.74.2632. URL: <http://dx.doi.org/10.1103/PhysRevLett.74.2632>.
- [2] F. Abe et al. “Observation of Top Quark Production in $p^- p$ Collisions with the Collider Detector at Fermilab”. In: *Physical Review Letters* 74.14 (Apr. 1995), pp. 2626–2631. ISSN: 1079-7114. DOI: 10.1103/physrevlett.74.2626. URL: <http://dx.doi.org/10.1103/PhysRevLett.74.2626>.
- [3] ATLAS. *ATLAS experiment - Episode 2 - The Particles Strike Back*. 2021. URL: <https://home.cern/resources/video/experiments/atlas-experiment-episode-2-particles-strike-back>.
- [4] *b-Jet Identification in the CMS Experiment*. Tech. rep. Geneva: CERN, 2012. URL: <https://cds.cern.ch/record/1427247>.
- [5] Miguel Castro Nunes Fiolhais. “Study of the Wtb Vertex Structure in Top Quark Decays with the ATLAS experiment and Future Prospects”. Presented 07 Mar 2013. Sept. 2012. URL: <https://cds.cern.ch/record/1544047>.
- [6] CERN. *ROOT Data Analysis Framework*. 2021. URL: <https://root.cern.ch/>.
- [7] ATLAS Collaboration. *Muon Spectrometer*. 2021. URL: <https://atlas.cern/discover/detector/muon-spectrometer>.

- [8] ATLAS Collaboration. *Muon Spectrometer*. 2021. URL: <https://atlas.cern/discover/detector/trigger-daq>.
- [9] ATLAS Collaboration. *The Inner Detector*. 2021. URL: <https://atlas.cern/discover/detector/inner-detector>.
- [10] Andrzej Czarnecki, Jürgen G. Körner, and Jan H. Piclum. “Helicity fractions of W bosons from top quark decays at next-to-next-to-leading order in QCD”. In: *Physical Review D* 81.11 (June 2010). ISSN: 1550-2368. DOI: 10.1103/physrevd.81.111503. URL: <http://dx.doi.org/10.1103/PhysRevD.81.111503>.
- [11] Lyndon Evans and Philip Bryant. “LHC Machine”. In: *Journal of Instrumentation* 3.08 (Aug. 2008), S08001–S08001. DOI: 10.1088/1748-0221/3/08/s08001. URL: <https://doi.org/10.1088/1748-0221/3/08/s08001>.
- [12] J. de Favereau et al. “DELPHES 3: a modular framework for fast simulation of a generic collider experiment”. In: *Journal of High Energy Physics* 2014.2 (Feb. 2014). ISSN: 1029-8479. DOI: 10.1007/jhep02(2014)057. URL: [http://dx.doi.org/10.1007/JHEP02\(2014\)057](http://dx.doi.org/10.1007/JHEP02(2014)057).
- [13] H. Fritzsch, M. Gell-Mann, and H. Leutwyler. “Advantages of the color octet gluon picture”. In: *Physics Letters B* 47.4 (1973), pp. 365–368. ISSN: 0370-2693. DOI: [https://doi.org/10.1016/0370-2693\(73\)90625-4](https://doi.org/10.1016/0370-2693(73)90625-4). URL: <https://www.sciencedirect.com/science/article/pii/0370269373906254>.
- [14] M. Gell-Mann. “A schematic model of baryons and mesons”. In: *Physics Letters* 8.3 (1964), pp. 214–215. ISSN: 0031-9163. DOI: [https://doi.org/10.1016/S0031-9163\(64\)92001-3](https://doi.org/10.1016/S0031-9163(64)92001-3). URL: <https://www.sciencedirect.com/science/article/pii/S0031916364920013>.
- [15] Julie Haffner. “The CERN accelerator complex. Complexe des accélérateurs du CERN”. In: (Oct. 2013). General Photo. URL: <http://cds.cern.ch/record/1621894>.
- [16] G. L. Kane, G. A. Ladinsky, and C. -P. Yuan. “Using the top quark for testing standard-model polarization and CP predictions”. In: *Phys. Rev. D* 45 (1 Jan. 1992), pp. 124–141. DOI: 10.1103/PhysRevD.45.124. URL: <https://link.aps.org/doi/10.1103/PhysRevD.45.124>.
- [17] Emmy Noether. “Invariant variation problems”. In: *Transport Theory and Statistical Physics* 1.3 (Jan. 1971), pp. 186–207. ISSN: 1532-2424. DOI: 10.1080/00411457108231446. URL: <http://dx.doi.org/10.1080/00411457108231446>.

- [18] *Optimisation of the ATLAS b-tagging performance for the 2016 LHC Run*. Tech. rep. All figures including auxiliary figures are available at <https://atlas.web.cern.ch/Atlas/GROUPS/PHYSICS/PUBNOTES/ATL-PHYS-PUB-2016-012>. Geneva: CERN, June 2016. URL: <https://cds.cern.ch/record/2160731>.
- [19] *Overview of the MC samples released in the 13 TeV ATLAS Open Data*. 2021. URL: <http://opendata.atlas.cern/release/2020/documentation/datasets/mc.html>.
- [20] Joao Pequenao. “Computer generated image of the whole ATLAS detector”. Mar. 2008. URL: <http://cds.cern.ch/record/1095924>.
- [21] Bogdan Povh et al. *Particles and Nuclei*. Springer Berlin Heidelberg, 2015. DOI: 10.1007/978-3-662-46321-5. URL: <https://doi.org/10.1007/978-3-662-46321-5>.
- [22] *Review of the 13 TeV ATLAS Open Data release*. Tech. rep. ATL-OREACH-PUB-2020-001. Geneva: CERN, Jan. 2020. URL: <https://cds.cern.ch/record/2707171>.
- [23] Pedro Ferreira da Silva. *Top quark production at the LHC*. 2016. arXiv: 1605.05343 [hep-ex].
- [24] Xabier Cid Vidal and Ramon Cid Manzano. *Momentum: Taking a closer look at LHC*. 2021. URL: https://www.lhc-closer.es/taking_a_closer_look_at_lhc/0.momentum.
- [25] C. S. Wu et al. “Experimental Test of Parity Conservation in Beta Decay”. In: *Phys. Rev.* 105 (4 Feb. 1957), pp. 1413–1415. DOI: 10.1103/PhysRev.105.1413. URL: <https://link.aps.org/doi/10.1103/PhysRev.105.1413>.
- [26] A. Zee. *Group Theory in a Nutshell for Physicists*. Princeton University Press, Mar. 2016. ISBN: 0691162697. URL: <https://www.xarg.org/ref/a/0691162697/>.
- [27] P.A. Zyla et al. “Review of Particle Physics”. In: *PTEP* 2020.8 (2020), p. 083C01. DOI: 10.1093/ptep/ptaa104.